

by the deep-penetrating faults (8). Our interpretation suggests that the ongoing formation of the mountain of Taiwan is coupled with the subduction through shearing. The coupling might be spatially heterogeneous and evolve in time as subduction progresses to collision.

REFERENCES AND NOTES

1. V. Schulte-Pelkum *et al.*, *Nature* **435**, 1222–1225 (2005).
2. J. Nabelek *et al.*, *Science* **325**, 1371–1374 (2009).
3. C. Beaumont, R. A. Jamieson, M. H. Nguyen, S. Medvedev, *J. Geophys. Res.* **109**, B06406 (2004).
4. T. Byrne *et al.*, The arc-continent collision in Taiwan, in *Arc-Continent Collision, Frontiers in Earth Sciences*, D. Brown, P. Ryan, Eds. (Springer-Verlag, Berlin, 2011), pp. 213–245.
5. D. Davis, J. Suppe, F. A. Dahlen, *J. Geophys. Res.* **88**, 1153–1172 (1983).
6. S. Carena, J. Suppe, H. Kao, *Geology* **30**, 935 (2002).
7. F. Wu, R.-J. Rau, D. Salzberg, *Tectonophysics* **274**, 191–220 (1997).
8. E. A. Bertrand *et al.*, *J. Geophys. Res.* **117**, B01402 (2012).
9. F. T. Wu, H. Kuo-Chen, K. D. McIntosh, *J. Asian Earth Sci.* **90**, 173–208 (2014).
10. P. G. Silver, *Annu. Rev. Earth Planet. Sci.* **24**, 385–432 (1996).
11. H. Kuo-Chen, F. T. Wu, D. Okaya, B.-S. Huang, W.-T. Liang, *Geophys. Res. Lett.* **36**, L12303 (2009).
12. W. Huang *et al.*, *J. Geophys. Res.* **105** (B12), 27979–27989 (2000).
13. T.-Y. Huang, Y. Gung, W.-T. Liang, L.-Y. Chiao, L. S. Teng, *Geophys. Res. Lett.* **39**, L05305 (2012).
14. L.-Y. Chiao, B.-Y. Kuo, *Geophys. J. Int.* **145**, 517–527 (2001).
15. Materials and methods are available as supplementary materials on Science Online
16. H.-H. Chen, Y.-H. Chen, H.-Y. Yen, G.-K. Yu, *Earth Planets Space* **55**, 223–230 (2003).
17. R. L. Rudnick, S. Gao, Composition of the continental crust, in *Treatise of Geochemistry 2nd ed.*, H. Holland, K. Turekian, Eds. (Elsevier, Amsterdam, 2014).
18. D. J. Tatham, G. E. Lloyd, R. W. H. Butler, M. Casey, *Earth Planet. Sci. Lett.* **267**, 118–128 (2008).
19. D. Mainprice, A. Nicolas, *J. Struct. Geol.* **11**, 175–189 (1989).
20. H. Kuo-Chen *et al.*, *Geophys. Res. Lett.* **39**, L22302 (2012).
21. Y.-J. Hsu, S.-B. Yu, M. Simons, L.-C. Kuo, H.-Y. Chen, *Tectonophysics* **479**, 4–18 (2009).
22. W. G. Ernst, *J. Metamorph. Geol.* **1**, 305–329 (1983).
23. M. Simoes *et al.*, *J. Geophys. Res.* **112**, B11405 (2007).
24. P. Yamato, F. Mouthereau, E. Burov, *Geophys. J. Int.* **176**, 307–326 (2009).
25. Y.-H. Lee *et al.*, *Geology* **43**, 451–454 (2015).
26. C.-S. Ho, *An Introduction to the Geology of Taiwan* (Central Geological Survey, Taiwan, 1999).
27. B. Rousset, S. Barbot, J.-P. Avouac, Y.-J. Hsu, *J. Geophys. Res.* **117**, B12405 (2012).

ACKNOWLEDGMENTS

We thank W.-T. Liang, F. T. Wu, K.-L. Wang, T.-F. Yui, W.-S. Chen, and J. Suppe for helpful discussions and comments. T. Byrne helped clarify the geological implications in an early draft and provided inspiring discussion. We thank three reviewers for their critical comments. We acknowledge the Taiwan Integrated Geodynamics Research (TAIGER) project, The Taiwan Earthquake Research Data Center (TECDC), Broad-Band Array in Taiwan for Seismology (BATS), and Central Weather Bureau Broad-Band array (CWBAB) for providing continuous broadband seismic waveforms. This work was supported by the Ministry of Science and Technology of Taiwan (MOST 103-2116-M-002-026) and Academia Sinica, Taiwan (AS-104-TP-A04). All the data used in this study are available in the following websites: CWBBB: <http://gdmis.cwb.gov.tw/index.php>; BATS: <http://bats.earth.sinica.edu.tw>; TAIGER: <http://ds.iris.edu/mda/YM?timewindow=2006-2009>.

SUPPLEMENTARY MATERIALS

www.sciencemag.org/content/349/6249/720/suppl/DC1
Materials and Methods
Supplementary Text
Figs. S1 to S12
Tables S1 and S2
References (28–35)

24 March 2015; accepted 30 June 2015
10.1126/science.aab1879

2D MATERIALS

Observation of tunable band gap and anisotropic Dirac semimetal state in black phosphorus

Jimin Kim,¹ Seung Su Baik,^{2,3} Sae Hee Ryu,^{1,4} Yeongsup Sohn,^{1,4} Soohyung Park,² Byeong-Gyu Park,⁵ Jonathan Denlinger,⁶ Yeonjin Yi,² Hyoung Joon Choi,^{2,3} Keun Su Kim^{1,4*}

Black phosphorus consists of stacked layers of phosphorene, a two-dimensional semiconductor with promising device characteristics. We report the realization of a widely tunable band gap in few-layer black phosphorus doped with potassium using an in situ surface doping technique. Through band structure measurements and calculations, we demonstrate that a vertical electric field from dopants modulates the band gap, owing to the giant Stark effect, and tunes the material from a moderate-gap semiconductor to a band-inverted semimetal. At the critical field of this band inversion, the material becomes a Dirac semimetal with anisotropic dispersion, linear in armchair and quadratic in zigzag directions. The tunable band structure of black phosphorus may allow great flexibility in design and optimization of electronic and optoelectronic devices.

Two-dimensional (2D) atomic crystals have continued to show great potential for application in nanoscale devices (1). A key issue is controlling their electronic states to overcome the limit of natural properties. Graphene's effectively massless state of charge carriers is a result of the conical band structure (2). However, the lack of a band gap (E_g) limits the on-off current ratio in planar field-effect transistors (3, 4), and it has been difficult to reliably achieve a sizable E_g without degrading its electronic quality (5–7). It would thus be desirable to realize a 2D system with a widely tunable E_g .

A potential candidate is few-layer black phosphorus (BP), a layered material of elemental phosphorus (5–22). The single-layer BP (or phosphorene) has a honeycomb network similar to graphene but is strongly puckered (armchair-shaped along x and zigzag-shaped along y in Fig. 1A), rendering its electronic state highly susceptible to external perturbations (11–22). The low-energy band structure of phosphorene can be approximated by a bonding and antibonding pair of mainly $3p_z$ orbitals (11, 12). The corresponding valence band (VB) and conduction band (CB) are located at the zone center (Γ_2^+ and Γ_4^- states in Fig. 1B) with the predicted E_g of 0.7 to 1.6 eV (13–17). For multilayers, the introduction of interlayer coupling reduces E_g with increasing film thickness and reaches ~0.33 eV in bulk BP (11–14). The E_g

of BP films and nanoribbons has been widely predicted to be tunable by strain (15–17) and electric field (17–21), the latter of which is more viable in gated devices. The electric field affects the real-space distribution of VB and CB states to be shifted in opposite directions to each other. Their potential difference and band mixing lead to a reduction in E_g , which is often termed the giant Stark effect (23–26). However, despite its potential importance for device applications, little is known experimentally about this effect on the surface of 2D semiconductors under a vertical electric field.

Here we report the realization of a widely tunable E_g in BP by means of the in situ deposition of potassium (K) atoms, the well-known technique to induce doping and electric field in 2D van der Waals systems (27). The K atoms on BP donate charges to the few top phosphorene layers, which are confined to form 2D electron gas near the surface (Fig. 1A, bottom). The band structure measured by angle-resolved photoemission spectroscopy (ARPES) at low K density is slightly n-doped with E_g greater than 0.6 eV (Fig. 1C). With increasing dopant density, the electric field from the ionized K donors gradually reduces E_g owing to the giant Stark effect, as supported by our density functional theory (DFT) calculations. Consequently, the electronic state of BP is widely and continuously tuned from a moderate-gap semiconductor to a band-inverted semimetal. At the critical dopant density of this band-inverted transition (21, 22), the electronic state becomes an anisotropic Dirac semimetal (Fig. 1D). This control mechanism of E_g should work in dual-gate BP devices for precisely balancing between high mobility and moderate E_g .

Figure 1, E to H, shows a series of ARPES spectra taken along the armchair direction k_x with different dopant density near direct E_g . As expected for pristine BP (28, 29), in Fig. 1E there

¹Department of Physics, Pohang University of Science and Technology, Pohang 790-784, Korea. ²Department of Physics, Yonsei University, Seoul 120-749, Korea. ³Center for Computational Studies of Advanced Electronic Material Properties, Yonsei University, Seoul 120-749, Korea. ⁴Center for Artificial Low Dimensional Electronic Systems, Institute for Basic Science, Pohang 790-784, Korea. ⁵Pohang Accelerator Laboratory, Pohang University of Science and Technology, Pohang 790-784, Korea. ⁶Advanced Light Source, Lawrence Berkeley National Laboratory, Berkeley, CA 94720, USA.

*Corresponding author. E-mail: keunsukim@postech.edu

is a well-defined VB with a nearly parabolic dispersion and with a vertex at 0.15 eV below the Fermi energy E_F (30). Assuming the reported E_g of 0.33 eV (12), our pristine sample is slightly hole-doped, which explains p-type conduction in transport (12). We use a k - p perturbation formula (31), widely accepted to fit the band dispersion of narrow-gap semiconductors, to quantify the hole effective mass m_x^* . The best fit (white line overlaid) yields $m_x^* = 0.08 \pm 0.03 m_e$, where m_e is the electron rest mass, in good agreement with theoretical calculations (12, 14).

Upon electron doping by the K deposition on the surface, the overall band structure rigidly shifts down toward high energies (fig. S2), so that the magnitude of E_g can be directly measured by ARPES. The energy shift of surface bands is accompanied by steep band bending toward the bulk (along z in Fig. 1A) to form 2D electronic states in a few phosphorene layers, as confirmed by little k_z dependence (31). At low dopant density just before the CB minimum drops below E_F (Fig. 1F), the VB rigidly shifts down, and E_g can be estimated at ~ 0.6 eV or slightly greater. This

E_g of 2D electronic states is smaller than that predicted for monolayer phosphorene (13–17) and is comparable to those predicted for few-layer phosphorene (0.3 to 1.0 eV) (13, 14). With further increasing dopant density, this E_g gradually reduces (Fig. 1G) and becomes zero (Fig. 1H), which indicates a semiconductor-semimetal transition. At the critical dopant density for this transition, where the VB and CB touch each other, the band dispersion in the armchair direction k_x becomes linear (Fig. 1H), whereas that in the zigzag direction k_y remains nearly parabolic (fig. S3).

The linear dispersion in k_x can be more clearly identified in high-resolution ARPES data (Fig. 2A). The peak positions follow X-shaped linear bands of the VB (red) and CB (blue) with a crossing point (Fig. 2C) that is also revealed in the intensity map at the crossing energy (Fig. 2E). The spectral simulation with linear bands and finite broadening (31) (Fig. 2B) successfully reproduces the experimental data in Fig. 2A. This suggests that BP at the critical density has a spin-degenerate Dirac state as in graphene (3) and Dirac semimetals (21, 32–34), which can be stabilized by crystalline symmetry, as explained below. A linear fit yields the velocity of charge carriers $v_x = 5.1 \pm 0.9 \times 10^5$ m/s, which is about half of that in graphene (2). Fig. 2, D to G, shows a series of constant-energy intensity maps. The ARPES intensity of band contours is modulated by the matrix-element effect that reflects the symmetry of constituent wave functions in real space (5). The maps above and below the energy of the Dirac point E_D (Fig. 2, D and F) show strong suppression along k_y with respect to k_x . The resultant twofold symmetry of intensity patterns confirms that they originate from BP rather than from K. Taking this matrix-element effect into account, the band contours are oval-shaped with the aspect ratio $r \sim 1.9$, which is related to armchair-zigzag anisotropy in Fig. 1A. Around the contour, the band dispersion gradually changes from linear along k_x to quadratic along k_y (fig. S4). These results support the picture of the anisotropic band crossing (Fig. 1D),

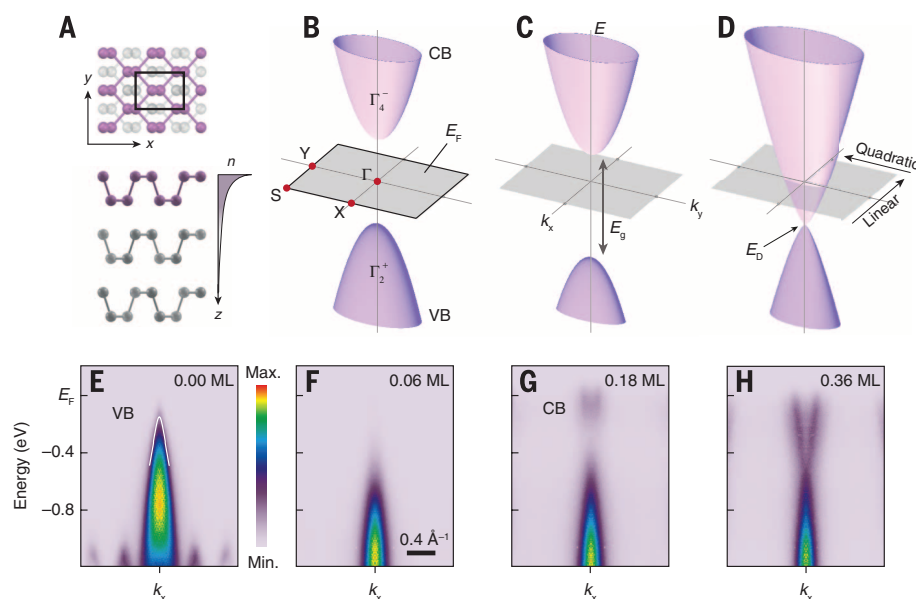
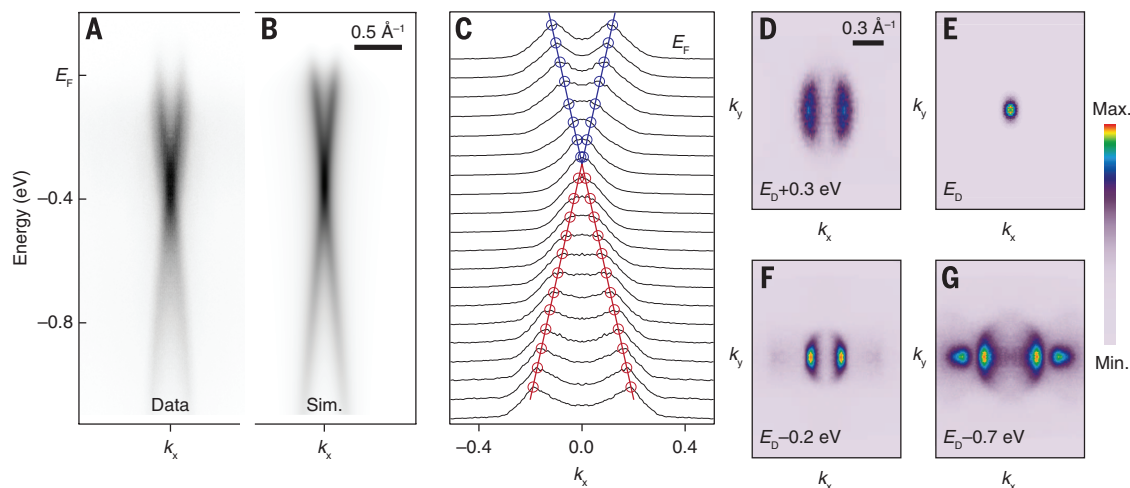


Fig. 1. Band structure and tunable E_g of few-layer BP. (A) (Top) Atomic structure of BP. The solid square is the surface unit cell, and the interlayer distance is ~ 5 Å. (Bottom) Density profile of a 2D electron gas decaying along z toward the bulk. (B to D) Band structure of (B) pristine BP, (C) BP in the initial stage of surface doping, and (D) BP at the transition to a zero-gap semimetal. The solid square in (B) indicates the surface Brillouin zone with high symmetry points marked by red circles. (E to H) Experimental band structure of BP taken at 15 K near E_F along k_x with dopant density marked at the upper right of each panel. The photon energy is 104 eV for k_z at the Z point of the bulk Brillouin zone (29). The dopant density is estimated in units of monolayers from simultaneously taken K 3p core-level spectra (fig. S7). The white line overlaid in (E) is a fit to the VB with the k - p perturbation formula (31).

Fig. 2. Anisotropic Dirac semimetal state at the critical density.

(A) High-resolution ARPES data taken at 15 K along the armchair direction k_x . (B) Corresponding spectral simulation with two linearly crossing bands and finite broadening (31). (C) Normalized momentum-distribution curves (0.05-eV steps from E_F) with their peak positions marked by open circles. Red and blue lines are linear fits to the VB and CB, respectively. (D to G) Series of ARPES intensity maps at constant energies (marked at the bottom of each panel), shown over a whole surface Brillouin zone (Fig. 1B).



which is reproduced by DFT calculations, as shown below.

To systematically follow the evolution of the band structure, we display a 3D representation of ARPES spectra as a function of dopant density N in Fig. 3A. The constant-energy cut at E_F shows that the Fermi momentum k_F of the CB steadily increases. We estimate the electron concentration n based on Luttinger's theorem as $\pi k_F^2 r$ that corresponds to the area enclosed by oval-shaped contours at E_F . We found that n is linearly proportional to N (fig. S6), which indicates monotonic charge transfer from dopants to phosphorene layers. In the constant-momentum cut at $k_x = 0$, diamonds and circles denote the positions of the VB maximum (E_V) and CB minimum (E_C), respectively. At the initial stage of doping, the Γ_2^+ state at E_V has rapidly shifted down until the Γ_4^- state at E_C drops below E_F . As N is increased further, the center energy $E_0 = (E_V + E_C)/2$ slowly shifts down, whereas the Γ_2^+ and Γ_4^- states get progressively closer to each other and eventually cross at the critical density $N_c = 0.36$ monolayers (ML) ($n = 8.3 \times 10^{13} \text{ cm}^{-2}$), where band inversion occurs. The magnitude of E_g is calculated as $E_C - E_V$ and is plotted as a function

of N in Fig. 3B. As can be seen from the figure, E_g is widely and continuously tunable in the range of +0.6 to -0.2 eV.

We performed DFT calculations based on four-layer BP with a single K atom on each 2-by-2 surface unit cell (corresponding to $N \sim 0.4$ ML in experiments). To effectively describe a lower K density, we increase the vertical distance d between K and BP (2.76 Å at equilibrium) such that the effect of K donors is gradually reduced without change in the supercell size ($3I$). A series of band calculations as a function of d reproduces key aspects of our experimental observations, the variation of E_g and resultant semimetal-semiconductor transition (red circles in Fig. 3B). Furthermore, at $E_g \sim 0$ ($d = 3.67$ Å), the bands along k_x are linearly dispersing near E_D , whereas those along k_y remain parabolic (Fig. 3C), as observed experimentally. N_c in Fig. 3B corresponds to the critical point of the band-inverted transition, where the topological invariant quantity Z_2 switches between 0 and 1 (21), induced by electric field rather than spin-orbit interaction. At this quantum critical point, the system is predicted to be in an unusual Dirac semimetal state (32) in which the band crossing along the rotational sym-

metry axis (the y axis, zigzag) is quadratic, whereas that along the other axis (the x axis, armchair) is linear. Our results thus collectively identify the formation of the anisotropic Dirac semimetal state at N_c , resulting from the characteristic puckered structure of phosphorene.

We now discuss the control mechanism of E_g . Figure 3D shows partial charge densities of E_V and E_C points in Fig. 3C, separated by a tiny gap (less than 10 meV) to avoid their degeneracy. The spatial distributions of E_V and E_C states, which are uniform in pristine BP (fig. S9), become strongly separated in opposite directions, indicating an electric field generated by the ionized K donors. The E_C states, which have a positive effective mass along z , freely move toward the positive electrical potential, whereas the E_V states, which have a negative effective mass along z , are pushed within the body of the BP layers (12). As stated above, this marked spatial separation of E_V and E_C states explains the variation of E_g by the giant Stark effect (17–21). Band calculations for four-layer BP under external electric field confirm the similar reduction in E_g (with no change in E_F) and the band crossover at the critical field of $\sim 0.19 \text{ V/Å}$. From this value, we quantify the Stark coefficient S_L for four-layer BP as $\sim 3 \text{ Å}$ (24), which is comparable to those predicted for few-layer BP (19, 21) and transition metal dichalcogenides (25, 26). Because S_L is known to increase with film thickness (19, 21), the critical field for bulk BP (or thicker BP films) would be smaller than the practical dielectric strengths of SiO_2 and $h\text{-BN}$. Our work thus demonstrates the giant Stark effect in BP as an efficient control mechanism of E_g , which is generally attainable in 2D semiconductors and devices composed of these materials.

REFERENCES AND NOTES

1. A. K. Geim, I. V. Grigorieva, *Nature* **499**, 419–425 (2013).
2. K. S. Novoselov et al., *Nature* **438**, 197–200 (2005).
3. A. K. Geim, *Science* **324**, 1530–1534 (2009).
4. L. Britnell et al., *Science* **335**, 947–950 (2012).
5. K. S. Kim et al., *Nat. Mater.* **12**, 887–892 (2013).
6. E. S. Reich, *Nature* **506**, 19 (2014).
7. H. O. Churchill, P. Jarillo-Herrero, *Nat. Nanotechnol.* **9**, 330–331 (2014).
8. L. Li et al., *Nat. Nanotechnol.* **9**, 372–377 (2014).
9. H. Liu et al., *ACS Nano* **8**, 4033–4041 (2014).
10. S. P. Koenig, R. A. Doganov, H. Schmidt, A. H. Castro Neto, B. Özyilmaz, *Appl. Phys. Lett.* **104**, 103106 (2014).
11. Y. Takao, H. Asahina, A. Morita, *J. Phys. Soc. Jpn.* **50**, 3362–3369 (1981).
12. A. Morita, *Appl. Phys.* **39**, 227–242 (1986).
13. A. N. Rudenko, M. I. Katsnelson, *Phys. Rev. B* **89**, 201408 (2014).
14. J. Qiao, X. Kong, Z.-X. Hu, F. Yang, W. Ji, *Nat. Commun.* **5**, 4475 (2014).
15. A. S. Rodin, A. Carvalho, A. H. Castro Neto, *Phys. Rev. Lett.* **112**, 176801 (2014).
16. X. Peng, Q. Wei, A. Copple, *Phys. Rev. B* **90**, 085402 (2014).
17. Y. Li, S. Yang, J. Li, *J. Phys. Chem. C* **118**, 23970–23976 (2014).
18. J. Dai, X. C. Zeng, *J. Phys. Chem. Lett.* **5**, 1289–1293 (2014).
19. H. Guo, N. Lu, J. Dai, X. Wu, X. C. Zeng, *J. Phys. Chem. C* **118**, 14051–14059 (2014).
20. Q. Wu, L. Shen, M. Yang, Z. Huang, Y. P. Peng, <http://arxiv.org/abs/1405.3077>.
21. Q. Liu, X. Zhang, L. B. Abdalla, A. Fazzio, A. Zunger, *Nano Lett.* **15**, 1222–1228 (2015).
22. R. Fei, V. Tran, L. Yang, *Phys. Rev. B* **91**, 195319 (2015).
23. K. H. Khoo, M. S. C. Mazzoni, S. G. Louie, *Phys. Rev. B* **69**, 201401 (2004).
24. F. Zheng, Z. Liu, J. Wu, W. Duan, B.-L. Gu, *Phys. Rev. B* **78**, 085423 (2008).

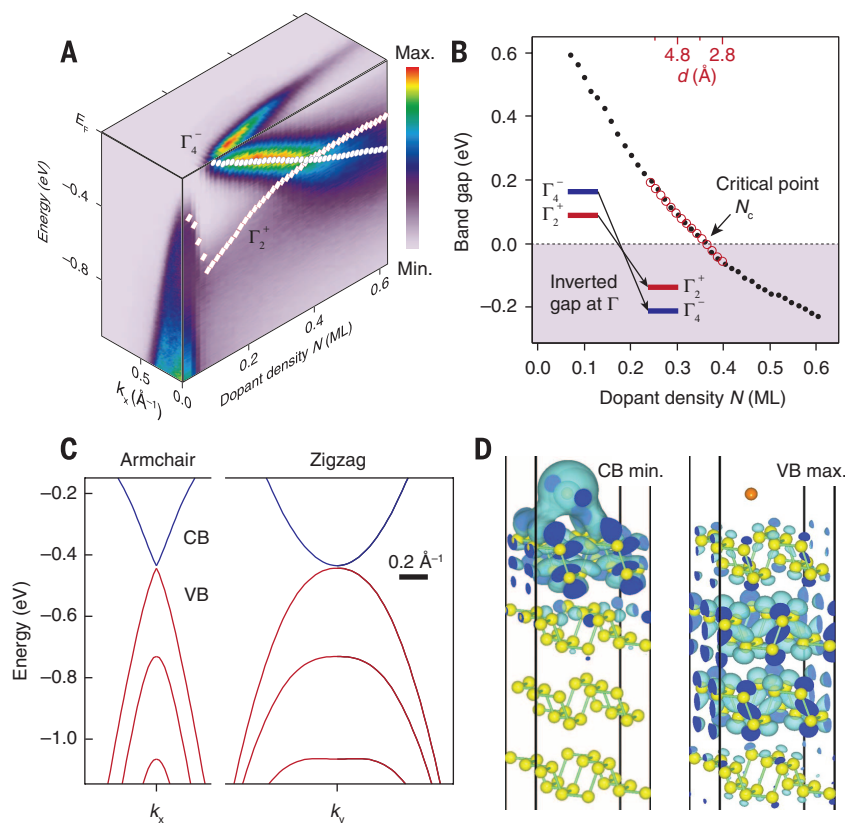


Fig. 3. Quantitative analysis for the control mechanism of E_g . (A) A 3D representation of the band evolution as a function of N , taken at 15 K. Diamonds and circles denote the positions of E_V and E_C , respectively. (B) E_g as a function of N . The negative gap in the shaded region represents the inverted gap at the Γ point. Overlaid red circles denote E_g from DFT band calculations where varying dopant density is simulated by changing the vertical distance d between K and BP (31). (C) Theoretical band dispersions for K-doped BP films at $d = 3.67$ Å. (D) Partial charge densities of E_V and E_C points in (C), separated by a tiny gap of less than 10 meV. Light blue areas represent the isosurface, set to $1.76 \times 10^{-3}/\text{Å}^3$, and its cross sections are shown in dark blue. Yellow and orange balls represent P and K atoms, respectively.

25. A. Ramasubramaniam, D. Naveh, E. Towe, *Phys. Rev. B* **84**, 205325 (2011).
26. Q. Yue *et al.*, *J. Phys. Condens. Matter* **24**, 335501 (2012).
27. T. Ohta, A. Bostwick, T. Seyller, K. Horn, E. Rotenberg, *Science* **313**, 951–954 (2006).
28. T. Takahashi, H. Tokailin, S. Suzuki, T. Sagawa, I. Shirohani, *Phys. Rev. B* **29**, 1105–1108 (1984).
29. C. Q. Han *et al.*, *Phys. Rev. B* **90**, 085101 (2014).
30. Note that continuum-like features in VBs vary with samples (see fig. S3), probably due to natural stacking disorder (5). Accordingly, the relative intensity of VBs and CBs is different for each cleaving of samples.
31. Materials and methods are available as supplementary materials on Science Online.

32. B.-J. Yang, N. Nagaosa, *Nat. Commun.* **5**, 4898 (2014).
33. Z. K. Liu *et al.*, *Science* **343**, 864–867 (2014).
34. X. Qian, J. Liu, L. Fu, J. Li, *Science* **346**, 1344–1347 (2014).

ACKNOWLEDGMENTS

This work was supported by IBS-R014-D1. S.S.B. and H.J.C. acknowledge support from the National Research Foundation of Korea (grant 2011-0018306). Computational resources have been provided by Korea Institute of Science and Technology Information Supercomputing Center (project KSC-2013-C3-062). S.P. and Y.Y. acknowledge support from the National Research Foundation of Korea (grant 2013R1A1A1A004778) and Yonsei University Future-Leading Research Initiative of 2014 (2014-22-0123). PLS-II was supported in part by the Ministry of Science, ICT and Future

Planning and Pohang University of Science and Technology. The Advanced Light Source was supported by the U.S. Department of Energy, Office of Sciences, under contract DE-AC02-05CH11231. We thank S. W. Jung, W. J. Shin, Y. K. Kim, and B. Kim for help with ARPES experiments.

SUPPLEMENTARY MATERIALS

www.sciencemag.org/content/349/6249/723/suppl/DC1
Materials and Methods

Figs. S1 to S9
References (35–41)

8 January 2015; accepted 14 July 2015
10.1126/science.aaa6486

APPLIED OPTICS

Voltage-tunable circular photogalvanic effect in silicon nanowires

Sajal Dhara,¹ Eugene J. Mele,² Ritesh Agarwal^{1*}

Electronic bands in crystals can support nontrivial topological textures arising from spin-orbit interactions, but purely orbital mechanisms can realize closely related dynamics without breaking spin degeneracies, opening up applications in materials containing only light elements. One such application is the circular photogalvanic effect (CPGE), which is the generation of photocurrents whose magnitude and polarity depend on the chirality of optical excitation. We show that the CPGE can arise from interband transitions at the metal contacts to silicon nanowires, where inversion symmetry is locally broken by an electric field. Bias voltage that modulates this field further controls the sign and magnitude of the CPGE. The generation of chirality-dependent photocurrents in silicon with a purely orbital-based mechanism will enable new functionalities in silicon that can be integrated with conventional electronics.

In the circular photogalvanic effect (CPGE), the polarity and magnitude of photocurrents can be controlled by the chirality of elliptically polarized optical excitation (P_{circ}) in a certain class of materials known as gyrotropic media. The effect originates from the unequal population of excited charged carriers in a preferential momentum direction when excited by light with left ($\sigma = -1$) or right ($\sigma = +1$) circular polarization. Semiconductors that support the CPGE are traditionally gyrotropic optical media with a strong spin-orbit coupling, so that the effect is ordinarily controlled by angular momentum selection rules for excitation with circularly polarized light. The effect has been observed in different quantum-well (QW) structures (1–5), for which it is attributed to the k -linear spin splitting of energy bands due to the spin-orbit interaction.

Most materials that have found widespread applications in conventional electronics (e.g., centrosymmetric crystals such as Si and Ge) are not gyrotropic and do not exhibit a bulk CPGE unless quantum-confined to below 10-nm length

scales. In Si/Ge QWs, a CPGE due to orbital (6, 7) or valley-orbital interactions (8), appears in the long wavelength range ($\sim 100 \mu\text{m}$). The underlying mechanism is attributed to intrasubband free carrier absorption pathways interfering with intersubband excitation (6) via polarizability effects. Photogalvanic effects have also been theoretically predicted in carbon nanotubes, without involving the electron spin degree of freedom (9). Because there are similarities between chiral nanotubes and Si nanowires (NWs) (10–12), it is desirable to determine whether centrosymmetric crystals of technologically important materials such as Si can also exhibit a CPGE when their shapes are engineered, thus adding novel functionalities.

We demonstrated a mechanism for the CPGE involving only the orbital degrees of freedom that are observed at the surface of Si NWs at the metal-NW junction. The atomic structure of the NW, along with the macroscopic field present at the contact, breaks the bulk symmetries allowing the CPGE. The $[110]$ surface of Si is of particular interest because of its high hole mobility (13–15) associated with a zigzag chain of atoms running along the $\langle 110 \rangle$ direction. A Schottky electric field along the NW $\langle 111 \rangle$ growth direction breaks the relevant mirror symmetries and produces a chiral structure, producing a CPGE that is tunable with applied bias.

Unintentionally doped Si NWs (diameter, 100 to 150 nm; grown mostly along the $\langle 111 \rangle$ direction and some along the $\langle 112 \rangle$ direction) were used to make two-terminal devices by electron-beam lithography [section 1 in (16)]. Figure 1A shows the schematic of the device and the measurement setup, where the laser [transverse electromagnetic (TEM_{00}) mode, wavelength 680 nm, spot size $\sim 2 \mu\text{m}$] is incident at the metal-NW junction [see (16) for details in section 1 and figs. S1 to S6]. The excitation energy (680 nm) of the laser is above the indirect bandgap of Si, and therefore contributions to the photocurrent from interband excitation (corresponding to the bulk of the Si NW) and the surface states on the $[1\bar{1}0]$ plane can be simultaneously present, albeit with different selection rules. Because of the geometrical anisotropy of NWs, the bulk contribution to photocurrent has two maxima with respect to linear polarization, owing to the preferential absorption of light polarized along the long axis (TM polarization) (17, 18) and in the perpendicular direction (TE polarization) to the NW at the metal-NW junction due to metal antenna effects (19, 20). In all of our experiments, we observed the usual linear polarization-dependent photocurrent variation as a function of the quarter-wave plate (QWP) [half-wave plate angle-dependent photocurrent variation is discussed in (16), sections 2 and 3 and fig. S8]. However, at the metal-NW junction, the most important contribution to the photocurrent came from the P_{circ} dependence, which we observed by noticing that the maximum change in the photocurrent appeared at the left-handed (45°) and right-handed (135°) circular polarization, which has a variation of $\sin(2\alpha)$ irrespective of the physical orientation of the NW device [(16), section 4 and fig. S9]. As a result, the observed photocurrent at room temperature of a representative device at an applied bias of 1 V at two different spatial positions, in the metal-NW contact region (Fig. 1B), and on the bare NW (far away from the contacts, Fig. 1C) displayed different polarization dependence. At the metal-semiconductor contact, the photocurrent pattern repeated twice [$\propto \sin(2\alpha)$] as the QWP angle was changed from 0° to 360° , whereas on the NW, the pattern repeated four times [$\sim \cos(4\alpha + \phi)$], with a phase term (ϕ) depending on the physical orientation of the NW and laser polarization], suggesting a strong P_{circ} -dependent photocurrent confined to the contact region. The photocurrents can be fitted (Fig. 1, B and C, solid line) with the expression $I(\alpha) = I_c \sin 2\alpha + I_l \cos(4\alpha + \phi) + I_d$, where I_c , I_l , and I_d are

¹Department of Materials Science and Engineering, University of Pennsylvania, Philadelphia, PA 19104, USA. ²Department of Physics and Astronomy, University of Pennsylvania, Philadelphia, PA 19104, USA.

*Corresponding author. E-mail: riteshag@seas.upenn.edu

This copy is for your personal, non-commercial use only.

If you wish to distribute this article to others, you can order high-quality copies for your colleagues, clients, or customers by [clicking here](#).

Permission to republish or repurpose articles or portions of articles can be obtained by following the guidelines [here](#).

The following resources related to this article are available online at www.sciencemag.org (this information is current as of August 23, 2015):

Updated information and services, including high-resolution figures, can be found in the online version of this article at:

<http://www.sciencemag.org/content/349/6249/723.full.html>

Supporting Online Material can be found at:

<http://www.sciencemag.org/content/suppl/2015/08/12/349.6249.723.DC1.html>

This article **cites 36 articles**, 6 of which can be accessed free:

<http://www.sciencemag.org/content/349/6249/723.full.html#ref-list-1>

This article appears in the following **subject collections**:

Physics

<http://www.sciencemag.org/cgi/collection/physics>